



# Rarefied gas flow through nanoscale tungsten channels



M.S. Ozhgibesov\*, T.S. Leu, C.H. Cheng

Department of Aeronautics and Astronautics, National Cheng Kung University, Tainan 701, Taiwan, ROC

## ARTICLE INFO

### Article history:

Accepted 26 February 2013

Available online 14 March 2013

### Keywords:

Molecular dynamics

Maxwell distribution

Argon–Tungsten interactions

Rarefied gas flow

Boundary conditions

## ABSTRACT

The aim of this work is to investigate argon flow behaviors through the channels with three types of boundary conditions. Current work deals with numerical simulations of rarefied gas flow through nano-channels using the Molecular Dynamics method. Taking into account that this method is very time consuming, we implemented all the simulations using CUDA capable graphic cards. We found that the well-known and relatively simple Maxwell model of boundary conditions is able to reproduce gas flow through a tungsten channel with irregularities and roughness, while it results in a significant error in the case of a smooth metal surface. We further found that the flow rate through a relatively short channel correlates nonlinearly with the channel's length. This finding is in contrast with the results available in extant literature. Our results are important for both numerical and theoretical analyses of rarefied gas flow in micro- and nano-systems where the choice of boundary conditions significantly influences flow.

Crown Copyright © 2013 Published by Elsevier Inc. All rights reserved.

## 1. Introduction

Improvements in micro fabrication as well as the resulting reductions in prices have increased the areas in which microsystems are applied [1]. This has motivated many engineers and researchers to develop micro-electro-mechanical-systems (MEMS). Such micro mechanisms can be applied in a wide range of applications, such as in micro biochemical reaction chambers [2], heat exchangers [3] and gas detectors [4]. Most of these devices deal with the flow of gases or liquids.

One of the earliest experimental studies of gas flow through a copper membrane was conducted by Warrick and Mack [5] in 1933. Hanks and Weissberg [6] proposed a semiempirical equation for the pressure driven flow through a circular channel. This relation was recently tested by Shinagawa et al. [7] who found it to be valid in the range of the continuum to the upper limit of the transition regime. There are many studies that have used both temperature and pressure driven flows through long channels since then, for example works [8,9,36], and Shen et al. [10].

Gas flow through extremely short channels (slits and orifices) has been intensively studied as well, for example the work of Lilly et al. [11] and Fujimoto and Usami [12]. Sreekanth [13] has also conducted experimental studies of rarefied gas flow through short metal channels in a wide range of pressure ratios. That paper

proposes the semiempirical equation for the estimation of the mass flow rate:

$$\dot{m} = \left[ \frac{\pi d_{ch}^4}{128 \mu R T_1} \frac{P_1 + P_2}{2} \Delta P + \frac{0.519}{\langle V_1 \rangle} \frac{d_{ch}^4}{L_{ch}} \right] \frac{1}{L_{ch}(1 + d_{ch}/L_{ch})}, \quad (1)$$

where  $\langle V \rangle$  is the average molecular velocity;  $\mu$  is the viscosity of the gas; and  $P$  and  $T$  is the pressure and temperature of the gas, respectively. Variables with subscripts 1 and 2 correspond to the parameters of gas in the upstream and downstream reservoirs. This relation was obtained for transition flows through extremely short tubes ( $L_{ch}/d_{ch} < 1$  length to diameter ratio).

The application of membranes to gas separation has been recently reviewed by Bernardo et al. [14]. Numerical or analytical investigations of gas flows through a membrane has normally been performed considering single channels or a small set of parallel channels with a further extrapolation of the results to the case of the membrane using correction factors [15]. Unfortunately, the real membranes may have highly curved or intersecting channels [16] making analysis of gas flow through such systems a complex issue. This problem can be solved by approximating the long curved/branched channel using a set of short channels ( $L_{ch}/d_{ch} \approx 1$ ) connected to each other. However, most extant studies have described gas flow through long straight channels or extremely short channels while discussions on middle-sized channels are almost nonexistent. Another problem is most of the theoretical studies on rarefied gas flow have been performed with an assumption of diffusive interactions between the gas atoms and channel surfaces; this approach may be valid for when the walls of the channels have imperfections (contaminations, scratches, etc.). On the other hand, the precision of MEMS manufacturing increases daily [17]. Results described by Leu et al. [18] show that a diffusive model

\* Corresponding author. Tel.: +886 6 2757575; fax: +886 6 2389940.  
E-mail address: [omiser@gmail.com](mailto:omiser@gmail.com) (M.S. Ozhgibesov).

is not able to reproduce all the processes accompanying collisions of gas atoms with clean and smooth metal surfaces.

The aim of this work is to study the behavior of argon flow through long and middle-sized channels in order to define the region of applicability of known relations presented by Sharipov [19], and Sharipov and Seleznev [20]. We have considered two different types of boundary conditions (BCs): specular–diffuse interactions (this model is commonly used in the above mentioned studies), and a channel with an atomic structure corresponding to the structure of tungsten. All investigations have been performed using the Molecular Dynamics (MD) simulations method. We observed that the choice of BC influences the flow properties and the significance grows with respect to the channel's length. Obtained results show that diffusive BCs represent a rough rather than a smooth wall. We further found that the flow rate depends nonlinearly on the channel's length in case of a short channel and tends to be linear with respect to the length for a longer channel. Another important impact of this paper is that we have defined the region of validity for the relations shown by Sharipov [19], and Sharipov and Seleznev [20] for predictions of mass flow rate.

## 2. Methodology

The physical model used in the current study is shown in Fig. 1. This 3D system consists of two rectangular tanks filled with argon with each their values of pressure and temperature,  $P_1, T_1$  and  $P_2, T_2$ , respectively. The argon flows between the tanks through the channel of square cross-section attached to the tank's wall. We found that the lateral dimensions of the tank must be at least 8 times greater than the corresponding size of the channel ( $H/h_{ch} \geq 8$ ); this guarantees that flow properties are not affected by the boundaries of the vessel. The pressure in the vessels was maintained at a constant value by adding new gas atoms to the left (right) quarter of the left (right) tank. Specular BCs were set up on the 5 faces of each tank, while the leftmost and the rightmost faces (ABCD and EFJK) were free of a boundary, i.e., the gas atoms were allowed to migrate through them. Atoms that passed through the plane ABCD or EFJK were excluded from the simulation. The total flow rate was estimated as follows:

$$J_{12} = \frac{\Delta N_{12} - \Delta N_{21}}{t}, \quad (2)$$

where  $\Delta N_{12}$  and  $\Delta N_{21}$  were the number of argon atoms that moved from the first vessel into the second one and vice versa, respectively, and  $t$  was the time elapsed from the start of the simulation. It should be noted that the positive value of  $J_{12}$  corresponds to the case when the flow from the left the tank exceeded the flow from the right one.

The results obtained for this flow configuration are discussed in terms of three parameters: the length-to-height ratio  $L_{ch}/h_{ch}$  of the

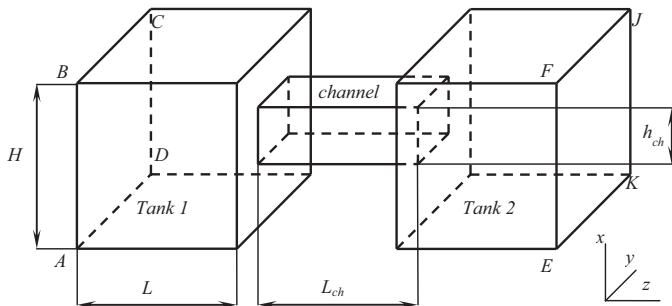


Fig. 1. Sketch of the system used for simulations.  $H$  and  $L$  are the height and length of the tanks, respectively;  $h_{ch}$  and  $L_{ch}$  are the height and length of the channel.

channel, the pressure ratio  $P_2/P_1$ , and the rarefaction parameter in term of Knudsen number [9] and viscosity [31], respectively:

$$\delta = \frac{\sqrt{\pi}}{2} \frac{h_{ch}}{\lambda} = \frac{\sqrt{\pi}}{2} \frac{1}{Kn} \quad \text{and} \quad \delta = \frac{h_{ch} P_0}{\mu_0 V_0}, \quad (3)$$

where  $\lambda$  is the molecular mean free path, and  $h_{ch}$  is the height of the channel;  $\mu_0$  and  $V_0$  are the shear viscosity of the gas and the most probable molecular speed at the temperature  $T_0$ .

One can see that the rarefaction parameter is inversely proportional to the Knudsen number, thus the limit  $\delta=0$  represents the free-molecular regime, while  $\delta \rightarrow \infty$  corresponds to the continuum regime.

The reduced flow rate  $W$  through the channel is defined as

$$W = \frac{J_{12}}{J_1}, \quad (4)$$

where  $J_1$  is the flow rate through the channel at any  $L_{ch}/h_{ch}$ ,  $P_2/P_1$  and  $\delta$ , and

$$J_1 = \frac{n_1 \langle V_1 \rangle}{4} h_{ch}^2. \quad (5)$$

This analytical equation expresses the flow rate through a square orifice ( $L_{ch}/h_{ch}=0$ ) into a vacuum ( $P_2/P_1=0$ ) at the free molecular regime.  $\langle V_1 \rangle$  is the average molecular speed at a given temperature  $T_1$  and  $n_1$  is the gas concentration.

We considered two types of BCs on the inner surfaces of the channel:

- The Maxwell model, also called diffuse–specular BC (two limiting cases were considered: full accommodation and the case of specular reflection);
- “Real channel,” i.e., a channel with walls represented by a set of tungsten atoms.

Implementation of the first BC was straightforward and has been discussed in many studies, for example [21]. The third channel was created by removing excess atoms from the tungsten bar (they were arranged according to the BCC structure of tungsten). This process is illustrated in Fig. 2a. Each wall of the channel consisted of six atomic layers, and atoms that comprised the outer layers were held fixed in their equilibrium lattice positions while the atoms in the other two layers were permitted to move according to the appropriate classical equations of motion. In order to demonstrate the influence of a channel's irregularities on flow, we considered two types of real channels with smooth (Fig. 2b – left picture) and wavy (Fig. 2b – right picture) walls, respectively. The initial velocities of the tungsten atoms were determined by the Maxwell distribution function corresponding to the desired temperature of the channel  $T_{ch}$ . The simple velocity scaling method was used to maintain the temperature of the tungsten at a constant value.

The interactions among the tungsten atoms were taken as being sums of pairwise Morse potential:

$$\Phi_{W-W} = \begin{cases} \varepsilon_W [e^{-2\beta_W(r-\sigma_W)} - 2e^{-\beta_W(r-\sigma_W)}], & 0 < r < 2.3\sigma_W \\ 0, & r \geq 2.3\sigma_W \end{cases}, \quad (6)$$

where the potential's parameters were [22]:  $\varepsilon_W = 0.9906$  eV,  $\beta_W = 14.116$  nm<sup>−1</sup>,  $\sigma_W = 0.3032$  nm.

To describe the interaction between an argon and tungsten atom, we applied the Lennard–Jones potential function:

$$\Phi_{W-Ar} = \begin{cases} 4\varepsilon_{WAr} \left[ \left( \frac{\sigma_{WAr}}{r} \right)^{12} - \left( \frac{\sigma_{WAr}}{r} \right)^6 \right], & 0 < r < 2.5\sigma_{WAr} \\ 0, & r \geq 2.5\sigma_{WAr} \end{cases}, \quad (7)$$

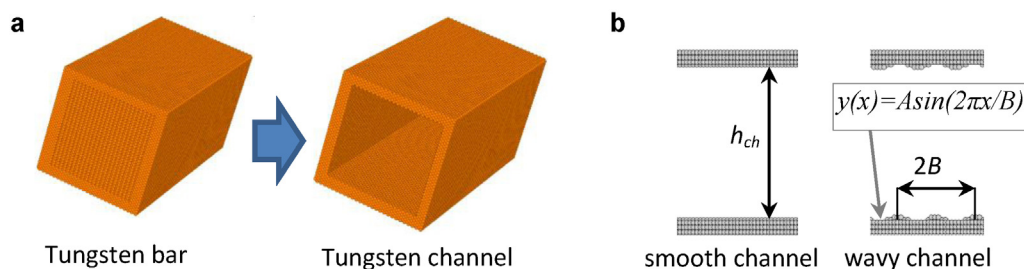


**Fig. 2.** (a) Sketch of the tungsten channel used for simulations. The tungsten channel (on the right) was created by removal of excess atoms of the tungsten bar (on the left). (b) Side view of the channels with smooth and wavy walls.  $B$  is the wavelength;  $h_{ch}$  is the height of the channel.

where the parameter values used were [34]:  $\varepsilon_{WAr}/k_B = 25.17$  K,  $\sigma_{WAr} = 2.93$  Å.

The Lennard–Jones 6–12 potential was also used to describe the argon–argon interactions, with the parameter  $\varepsilon_{Ar}/k_B = 119.18$  K. The adequacy of the chosen model for the interaction of argon atoms with tungsten has been discussed in detail in our previous work [23].

The second order velocity Verlet scheme [21] with a time step of  $\Delta t = 10^{-16}$  s (smaller than the characteristic time of atom interactions) was used to integrate the equations of motion. The computational process was continued until the net flux between the tanks did not become stable.

It should be noted that MD simulations are very time consuming. Similarly, processes related to rarefied gas flows are characterized by a long stabilization period after which the flow reaches a steady state regime. Until the mid-1990s most of the MD programs were sequential, but the development of parallel computational systems made a new turn in the development of molecular dynamics that allowed one to enlarge the simulated system. In comparison to desktop computers, computer clusters have greater computational power at the cost of higher electrical consumption and capital cost. The next turn in evolution of computational systems can be treated as the development of General Purpose Graphics Processing Units (GPGPU) and corresponding programming languages. NVIDIA has developed Compute Unified Device Architecture (CUDA) that allows one to use the power of Graphic Processing Units (GPU) for computations. Since their inception, GPUs have been used extensively in graphic intensive applications only. These devices are designed to reduce the load on the main processor (CPU) while rendering complicated 3D graphics. Almost all of these operations are well parallelizable, and consequently GPUs have the potential to become powerful tools for scientific computing.

Fortunately, MD algorithms are well-parallelizable due to their nature. The usage of GPUs for MD simulations is made further attractive due to their relatively low price, compact size and low power consumption compared to computer clusters. High-bandwidth memory and multithreading hardware implementation enable GPUs to outperform traditional CPU cores on data parallel workloads by factors ranging from 10 to 30 times faster in most cases [24], and up to as much as 100 times faster in a few ideal cases [25,26].

All simulations in the present study were performed using a program code developed by the authors of the current work, on a CUDA capable GPU. This parallel computation method allowed us to perform a vast number of system simulations involving up to several hundred thousand atoms.

The main feature of a GPU is that every multiprocessor executes the same list of instructions. Details of the GPUs' architecture are described in many papers [27–29]. Modern GPUs may have up to several hundred computational processors and a complicated memory architecture. Such a vast number of processors allow for simulations of huge semi-realistic systems using parallel

algorithms. It should, however, be noted that a “bottleneck” is produced by a relatively low data exchange rate between the host (the RAM of the computer) and the device (GPU) memory. Consequently, an ideal case suggests that all computations must be performed by a GPU only, or one should at least minimize all data exchanges between the host and GPU memories.

There are many different MD algorithms, but all of them include the following steps:

1. Data initialization,
2. Computation of forces acting on atoms, and
3. Integration of equations of motion.

The most time-consuming step is computing the force. It generally requires  $N^2$  operations ( $N$  pairwise interactions must be considered), but as long distance interactions can be ignored, the amount of required operations can be decreased. A sorting method, i.e., creating a list of atoms surrounding every instant atom, is used to reduce the amount of required operations. The MD algorithm based on the Verlet list sorting method was considered in the current paper. All computations were placed on a GPU, and the CPU was used just for current temperature estimations and data output purposes. A more detailed description of the implemented algorithm is presented in our previous work [30].

In the current work, we applied the OpenMP and CUDA technologies, the first allows us to share the job among the CPU cores, while the second provides us with the advantage of using the GPU for computations. The combination of these technologies allows one to share the job among several GPUs by using the CPU to control the exchanges between the GPUs. Thus each separate CPU core governs a separate GPU. We used two gaming graphic cards: NVIDIA GeForce GTX590 and GTX580. It should be noted that the GTX590 consists of two graphic cards that can work separately. We have thus used 3 of the CPU's cores to control both the GTX590 and the GTX580 GPUs. The total number of GPU cores involved in our simulations was 1536. Table 1 represents the normalized time of execution of the MD program on different computation systems. One can see that the parallel program run on CUDA GPUs outperforms the sequential one by about 130 times.

**Table 1**  
Normalized time of execution of the MD program on different computational systems.

Number of atoms	CPU (intel i7-950)		GTX590 + GTX580
	Sequential	OpenMP	CUDA + OpenMP
	1 CPU	4 CPUs	
14,894	52.20	22.99	1.00
34,461	155.78	68.73	2.98
66,326	416.34	173.22	5.17
178,956	2258.29	919.00	19.67
265,721	4703.86	1849.05	33.89

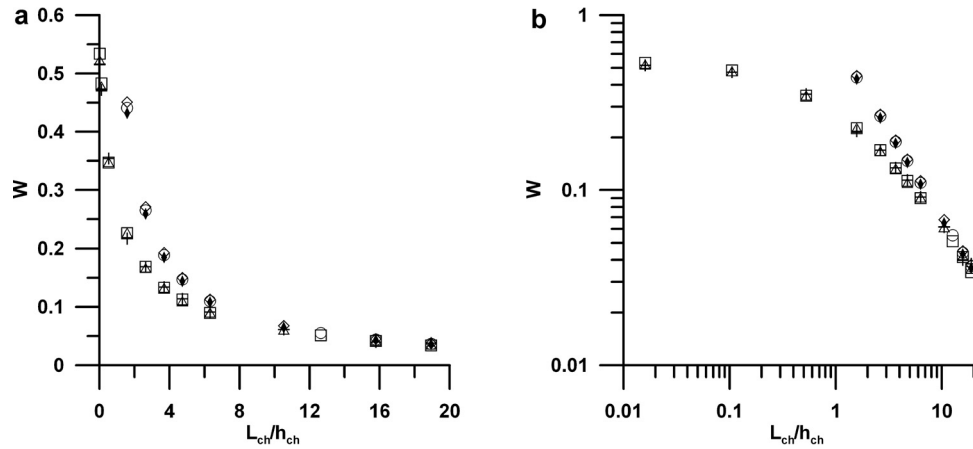


**Fig. 3.** (a) Normalized flow rate versus channel length-to-height ratio. Parameters of simulations:  $P_2/P_1 = 0.5$ ; diffusive BC,  $\delta = 0.1$  (current study);  $\diamond, \delta = 0.1$  (Sharipov [19]);  $\square, \delta = 0.2$  (current study);  $\circ, \delta = 0.2$  (Sharipov [19]);  $\triangle, \delta = 0.4$  (current study);  $\blacklozenge, \delta = 0.4$  (Sharipov [19]). (b) Normalized flow rate versus channel length-to-height ratio in a log–log scale. Parameters of simulations:  $P_2/P_1 = 0.5$ ; Maxwell BC (full accommodation),  $\delta = 0.1$  (current study);  $\diamond, \delta = 0.1$  (Sharipov [19]);  $\square, \delta = 0.2$  (current study);  $\circ, \delta = 0.2$  (Sharipov [19]);  $\triangle, \delta = 0.4$  (current study);  $\blacklozenge, \delta = 0.4$  (Sharipov [19]).

### 3. Results and discussion

First, we compared our results with data published earlier by other researchers. Fig. 3a represents the correlation between the dimensionless flow rate  $W$  versus the channel's length-to-height ratio. The two limiting cases,  $L_{ch}/h_{ch} = 0$  and  $L_{ch}/h_{ch} \gg 1$ , are discussed in articles by Sharipov and Kozak [31] and Sharipov [19], respectively. In the case of the orifice ( $L_{ch}/h_{ch} = 0$ ) we obtained  $W(\delta = 0.2) = 0.538$  and  $W(\delta = 0.1) = 0.517$ , while Sharipov and Kozak [31] reported  $W = 0.539$  and  $W = 0.520$ , respectively. The inequalities are less than 1%. The derivation of analytical expression that allows for the calculation of mass flow through long channels of rectangular cross sections to be completed was done by Sharipov [19]; this equation was derived with the assumption of a diffusive scattering of the gas atoms on the channel's walls. In the case of a long channel ( $L_{ch}/h_{ch} > 10$ ) our results coincide with the predictions made with the analytical expression by Sharipov [19]. These two issues allow us to conclude that the current model provides physically adequate results and can be used in further studies.

Another important consequence following from the observation of Fig. 3a is there is a nonlinear dependence between the flow rate and the channel's length in the case of a short channel ( $L_{ch}/h_{ch} < 10$ ). This phenomenon is clearly shown in Fig. 3b, which is similar to Fig. 3a, but in a log–log scale. One can see that the linear approximation becomes valid only if the channel is long enough ( $L_{ch}/h_{ch} > 10$ ). Consequently, the equations [19] are valid only if  $L_{ch}/h_{ch} > 10$ .

The correct choice of BC is one of the most important issues in simulations of rarified gas flows. According to the theoretical results [9] the flow rate decreases with respect to the accommodation coefficient on the channel's walls. Results discussed by Leu et al. [18] show that argon–tungsten interactions are more specular than diffusive, especially in cases of high incident energies of the gas. This statement is in accordance with the results shown in Table 2. The last column of Table 2 represents the flow rate through

the real channel with smooth walls is greater than the flow through the channel with a fully diffusive BC. One can see that this gap increases with respect to the channel's length. Such behavior can be explained in terms of the number of collisions between the gas atoms and the channel's walls. Thus, in the case of a long channel, the gas atoms experience more collisions than in the case of a short one. Consequently, the importance of BCs is proportional to the length of the channel. It should be noted that the interaction of the gas atoms with a solid surface can be described in terms of the probability of scattering in a forward/backward direction. This probability corresponds to the fraction of gas atoms that keep/change their direction after a collision with a surface. In the case of a single atom, the preservation of direction of movement takes place if the following dot product has a positive value:

$$V^{is} = \vec{V}^i \cdot \vec{V}^s, \quad (8)$$

where  $\vec{V}^i$  is the velocity of the gas atom before its collision with the surface, and  $\vec{V}^s$  is the velocity of the gas atom before it is scattered by the surface.

Fig. 4 shows how the fraction of atoms scattered backward depends on the parameters of the surface and Argon atom's incident

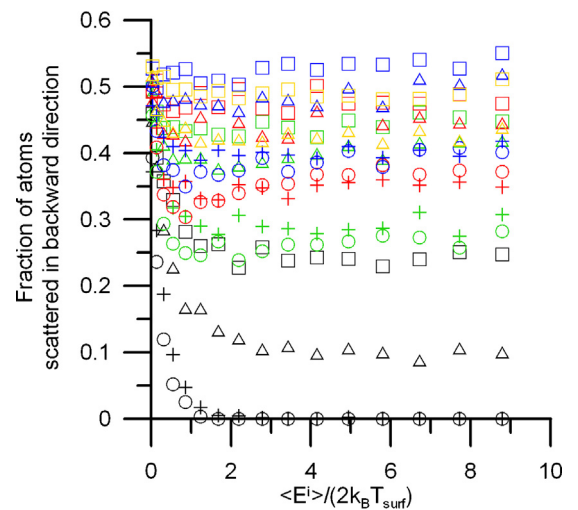


**Fig. 4.** Fraction of atoms scattered by a smooth tungsten surface in a backward direction versus the energy of the impinging Ar atoms.  $\square, \beta^i = 10^\circ$ ;  $\triangle, \beta^i = 20^\circ$ ;  $+, \beta^i = 40^\circ$ ;  $\circ, \beta^i = 60^\circ$ . The black symbols correspond to a smooth surface. The green, red, blue and yellow symbols correspond to Type B, C, D and E surfaces, respectively.

**Table 2**

Flow rate through the channel versus the length-to-height ratio.  $W_{real}$  is the flow rate through the real channel with smooth walls;  $W_{diff}$  is the flow rate through the channels with Maxwell BCs (in case of full accommodation).

$L_{ch}/h_{ch}$	$W_{real}$	$W_{diff}$	$\varepsilon$ (%)
0.55	0.388	0.343	13.3
1.08	0.309	0.265	16.6
2.68	0.206	0.170	20.9
4.80	0.144	0.116	24.1



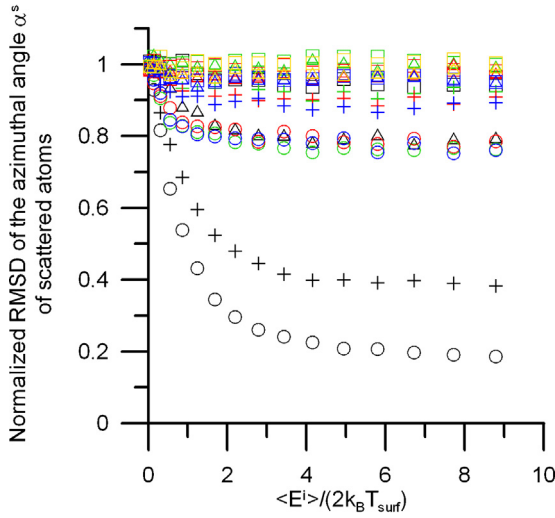


**Fig. 5.** Normalized root mean square deviation  $\sigma_\alpha$  of the azimuthal angle  $\alpha^s$  of scattered atoms versus kinetic energy of impinging atoms and incident polar angle.  $\square, \beta^i = 10^\circ$ ;  $\triangle, \beta^i = 20^\circ$ ;  $+, \beta^i = 40^\circ$ ;  $\circ, \beta^i = 60^\circ$ . Black symbols correspond to a smooth surface. Green, red, blue and yellow symbols correspond to surfaces of Types B, C, D and E, respectively. (For interpretation of the references to color in this figure legend, the reader is referred to the web version of this article.)

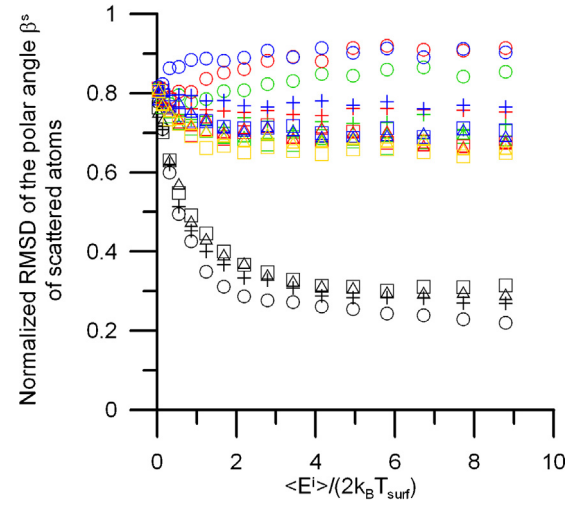


**Fig. 6.** Normalized root mean square deviation  $\sigma_\beta$  of the polar angle  $\beta^s$  of scattered atoms versus kinetic energy of impinging atoms and incident polar angle.  $\square, \beta^i = 10^\circ$ ;  $\triangle, \beta^i = 20^\circ$ ;  $+, \beta^i = 40^\circ$ ;  $\circ, \beta^i = 60^\circ$ . Black symbols correspond to a smooth surface. Green, red, blue and yellow symbols correspond to surfaces of Types B, C, D and E, respectively. (For interpretation of the references to color in this figure legend, the reader is referred to the web version of this article.)

angle  $\beta^i$  (this angle is measured with respect to the surface normal) and energy. In the case of diffuse BCs (shown by the solid line in Fig. 4), every gas atom is scattered in a forward direction with a probability of 50% (this value follows from the nature of diffuse BCs), regardless of the parameters before the collision, while in the case of a smooth tungsten surface this probability is usually greater than 50% and depends on the atom's parameters of incidence. The black symbols in Fig. 4 correspond to the case of a smooth tungsten surface. One can see that the fraction of atoms scattered in a backward direction is sufficient in the case of a low incident energy of the Ar atoms, and it decreases when the energy of the falling beam becomes higher. It should be noted that the probability of the atoms scattering in a forward direction depends on the angle of incidence  $\beta^i$  (this angle is measured with respect to the surface normal). These results are in accordance with results reported by Chase et al. [32]. The colored symbols in Fig. 4 correspond to the case of rough tungsten surfaces. One can see that surface imperfections increase diffusivity of the scattering, i.e., the reflection angle of the falling atom becomes non-dependent on the incident atom's parameters. This result is in line with discussions presented in [33,34]. Experimental data for atomically clean surfaces were reported in [33]. The data showed that the flow rate for such a surface is 25% larger than that for contaminated surface.

Figs. 5 and 6 represent the correlation of the normalized root-mean-square deviation (RMSD) of the azimuthal  $\alpha^s$  angle (this angle is measured with respect to the channel longitudinal axis) and the polar angle  $\beta^s$  of scattered atoms with energy and angle of incidence. Both polar and azimuthal angles of the scattered atoms were found to vary within the ranges of  $[-\pi/2; \pi/2]$ , thus the normalized RMSD corresponding to a uniform distribution for random numbers within this range was

$$\sigma_{uni} = \frac{b-a}{\sqrt{12}} = \frac{180}{\sqrt{12}} = 30\sqrt{3} \quad (9a)$$

and the normalized RMSDs of scattering of the scattering angles  $\alpha^s$  and  $\beta^s$ , respectively, can be defined as follows:

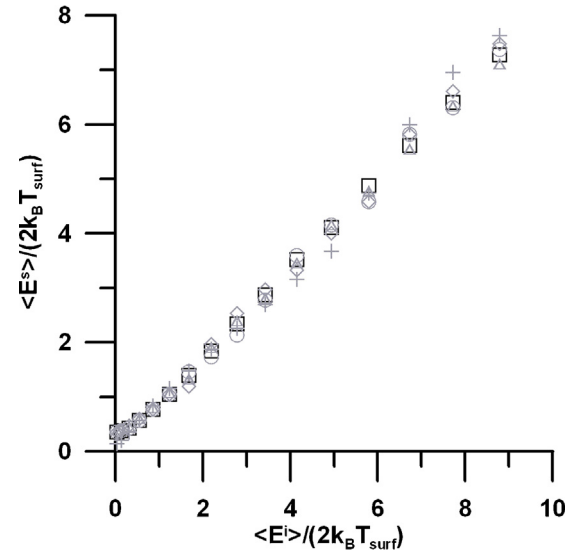
$$\bar{\sigma}_\alpha = \frac{\sigma_\alpha}{\sigma_{uni}} = \frac{\sigma_\alpha}{30\sqrt{3}}, \quad (9b)$$

$$\bar{\sigma}_\beta = \frac{\sigma_\beta}{\sigma_{uni}} = \frac{\sigma_\beta}{30\sqrt{3}}. \quad (9c)$$

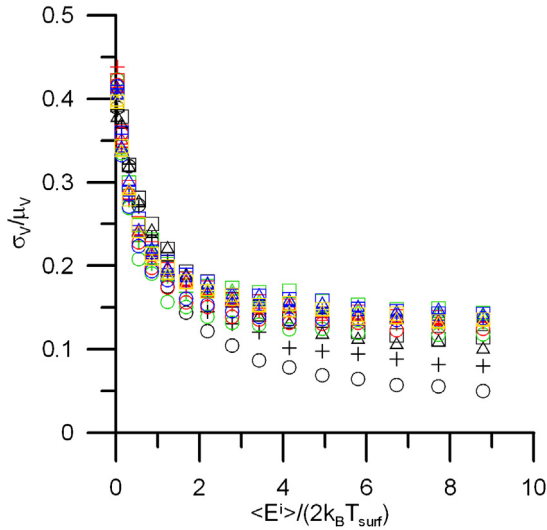
The black symbols in Figs. 5 and 6 correspond to a smooth surface. It is clear that the existence of imperfections on the surface turns the angular distribution of the scattered atoms from normal (discussions about angular distribution functions are shown in our previous work [18]) to uniform, i.e., the direction of the velocity vectors of the scattered atoms becomes independent of the parameters of incidence.

Fig. 7 illustrates the dependence between the energy of the scattered atoms and the incident kinetic energy of the gas atoms. The black and gray symbols correspond to the case of smooth and rough surfaces, respectively. The correlation between the kinetic energies shown in Fig. 5 can be approximated by the linear function:

$$\langle E^s \rangle = b_B \langle E^i \rangle + b_S(2k_B T_{surf}), \quad (10)$$



**Fig. 7.** Mean energy of scattered atoms versus energy of impinging atoms at  $\beta^i = 10^\circ$ .  $\square$ , real channel (Type A);  $\circ$ , real channel (Type B);  $\triangle$ , real channel (Type C);  $\diamond$ , real channel (Type D);  $+$ , real channel (Type E).



**Fig. 8.** Root mean square deviation of scattered atoms' velocities  $\sigma_V$  over mean velocity of scattered atoms  $\mu_V$  versus kinetic energy of impinging atoms.  $\square, \beta^i = 10^\circ$ ;  $\triangle, \beta^i = 20^\circ$ ;  $+, \beta^i = 40^\circ$ ;  $\circ, \beta^i = 60^\circ$ . Black symbols correspond to a smooth surface. Green, red, blue and yellow symbols correspond to surfaces of Types B, C, D and E, respectively. (For interpretation of the references to color in this figure legend, the reader is referred to the web version of this article.)

where  $k_B$  is the Boltzmann's constant, and  $b_S$  and  $b_B$  are the proportionality factors. In the case of an angle of incidence  $\beta^i = 45^\circ$ , the proportionality factors have values of  $b_S = 0.18$  and  $b_B = 0.77$ . The values of  $b_S$  and  $b_B$  have a 9% difference between similar parameters measured experimentally by Janda et al. [35]. This difference can be explained by the fact that even the best MD model is a rough approximation of a natural process. For example, the simulated model was ideal, i.e., the surfaces of the channel had no contaminations and the vacuum was perfect, while a real channel and vacuum may not be that ideal. Based on the above, we conclude that achieving a 9% difference is a reasonable result.

An analysis of Eq. (10) allowed us to conclude that if the energy of the incident beam was less than  $b_S(2k_B T_{surf})/(1 - b_B)$ , then the surface transferred energy to the gas ( $E^S > E^i$ ), otherwise the gas gave up energy to the surface ( $E^i > E^S$ ). One can see that data points corresponding to smooth and rough surfaces are very close to each other, which means that the roughness of the surface does not influence the average energy of the scattered gas atoms. However Fig. 8 shows that the ratio ( $\sigma_V/\mu_V$ ) of RMSD to the mean velocity of the atoms scattered by the surface is higher in the case of a rough surface when compared to a smooth one. If the distribution of random numbers corresponds to a Maxwell–Boltzmann distribution, the relationship between root-mean-square deviation (RMSD)  $\sigma$  and the mean value  $\mu$  would be described by the following relation:

$$\frac{\sigma}{\mu} = \frac{1}{2} \sqrt{\frac{3\pi - 8}{2}} \approx 0.42. \quad (11)$$

The last issue means that the distribution of the velocities of the scattered atoms becomes more Maxwell-like in the case of a rough surface. One can see that the value of  $\sigma_V/\mu_V$  more rapidly approaches 0.42 with decreasing incident energy, regardless of the incident polar angle  $\beta^i$ , in the case of an imperfect surface.

Data shown in Fig. 9 represent correlations between the flow rate and pressure difference for various types of BCs. Gray circles correspond to the results obtained experimentally by Sreekanth [13] and approximated using Eq. (1). One can see that first order polynomials can fit the data points perfectly, while the slope of the approximation line is a so-called hydrodynamics conductance (HC). Table 3 represents the HC values of the channels with various

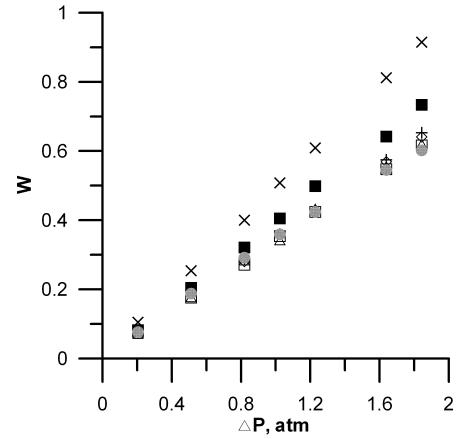


**Fig. 9.** Normalized flow rate versus pressure difference.  $\blacksquare$ , real channel (Type A);  $\diamond$ , real channel (Type B);  $\square$ , real channel (Type C);  $+$ , real channel (Type E);  $\triangle$ , Maxwell BC (full accommodation);  $\bullet$ , semi empirical eq. [13];  $\times$ , Maxwell BC (specular reflection).

**Table 3**

Hydrodynamic conductance of the channel with various BCs on the walls. Parameters  $A$  and  $B$  are the amplitude and wavelength of the roughness on the walls, respectively.

Channel type	$A$ ( $10^{-10}$ m)	$B$ ( $10^{-10}$ m)	$C_{hyd}$ ( $\text{atm}^{-1}$ )
Type A	0	–	0.3969
Type B	3.16	6.32	0.3485
Type C	1.58	6.32	0.3376
Type D	3.16	12.64	0.3313
Type E	1.58	12.64	0.3520
Diffuse BC			0.3410
Semi empirical eq. by Sreekanth [13]			0.3372
Specular BC			0.4955

BCs as well as explains the types of real channels mentioned above. It is obvious that channels with specular boundaries have the highest HC values. Furthermore, the HC value of clean and ideal tungsten channels (Type A) is greater than that of channels with diffuse BCs. Thus the interactions of argon with tungsten are found to be neither purely diffusive nor purely “mirror-like.” This observation is in line with results shown by Leu et al. [18] and Ozhgibesov et al. [23]. Another important result that can be observed in Table 3 is that the HC values correlate with the imperfection parameters in a very complicated manner. It is obvious that an increase of a wave's amplitude (Fig. 2b) should cause a decrease in the value of HC, but a comparison of the conductance of the Type B and Type C channels shows the opposite occurs. Lastly, Type E channels are more conductive than Type C, and thus the value of HC is in direct proportion with the wavelength of roughness. This means that an increase of wavelength causes a smoothing of the imperfections, and consequently a rise in the value of HC.

#### 4. Conclusion

This study investigated rarefied gas flow between two tanks and our results are in good agreement with the theoretical and experimental studies of other researches. However, the results of the MD simulations have shown that diffuse BCs represent rough rather than smooth walls. We further found that the known theoretical prediction of flow rate through channels with diffuse BCs is valid only if the length-to-height ratio is greater than 10, while in the case of a short channel, the dependence between flow rate and length is nonlinear.

We observed that the roughness of the surface significantly influences the momentum change caused by the collision of the

gas atoms with the tungsten wall. We further observed that the mean kinetic energy of the argon atoms scattered on the tungsten surface does not correlate with the roughness of the surface in the range of our studied parameters. However, the root-mean-square distribution of the velocities of the scattered atoms was found to be dependent on surface roughness.

We observed a discrepancy of 15% between the values of HC measured in the simulations of gas flow through the smooth tungsten channel and the conductivity obtained from our semi-empirical equation. We can conclude that the flow inside a channel produced with a high level of precision cannot be modeled using the assumption of a diffuse BC; a more complex BC model is required.

## References

- [1] B. Bhushan, Nanotribology and nanomechanics of MEMS/NEMS and BioMEMS/BioNEMS materials and devices, *Microelectronic Engineering* 84 (3) (2007) 387–412.
- [2] T. Fujii, PDMS-based microfluidic devices for biomedical applications, *Microelectronic Engineering* 61–62 (2002) 907–914.
- [3] G.S. Chung, J.M. Jeong, Fabrication of micro heaters on polycrystalline 3C–SiC suspended membranes for gas sensors and their characteristics, *Microelectronic Engineering* 87 (11) (2010) 2348–2352.
- [4] J. Zhou, P. Li, S. Zhang, Y. Huang, P. Yang, M. Bao, G. Ruan, Self-excited piezoelectric microcantilever for gas detection, *Microelectronic Engineering* 69 (1) (2003) 37–46.
- [5] D.L. Warrick, E. Mack, A copper membrane gas-molecule sieve. Callendar's theory of osmosis, *Journal of the American Chemical Society* 55 (4) (1933) 1324–1332.
- [6] R.W. Hanks, H.L. Weissberg, Slow viscous flow of rarefied gases through short tubes, *Journal of Applied Physics* 35 (1) (1964) 142–144.
- [7] H. Shinagawa, H. Setyawan, T. Asai, Y. Sugiyama, K. Okuyama, An experimental and theoretical investigation of rarefied gas flow through circular tube of finite length, *Chemical Engineering Science* 57 (19) (2002) 4027–4036.
- [8] I. Graur, F. Sharipov, Non-isothermal flow of rarefied gas through a long pipe with elliptic cross section, *Microfluidics and Nanofluidics* 6 (2) (2009) 267–275.
- [9] F. Sharipov, Rarefied gas flow through a long tube at any temperature ratio, *Journal of Vacuum Science and Technology A* 14 (4) (1996) 2627–2635.
- [10] C. Shen, J. Fan, C. Xie, Statistical simulation of rarefied gas flows in micro-channels, *Journal of Computational Physics* 189 (2) (2003) 512–526.
- [11] T.C. Lilly, S.F. Gimelshein, A.D. Ketsdever, G.N. Markelov, Measurements and computations of mass flow and momentum flux through short tubes in rarefied gases, *Physics of Fluids* 18 (9) (2006) 093601–093611.
- [12] T. Fujimoto, M. Usami, Rarefied gas flow through a circular orifice and short tubes, *Journal of Fluids Engineering* 106 (4) (1984) 367–373.
- [13] A. Srekanth, Transition flow through short circular tubes, *Physics of Fluids* 8 (11) (1965) 1951–1956.
- [14] P. Bernardo, E. Drioli, G. Golemme, Membrane gas separation: a review/state of the art, *Industrial and Engineering Chemistry Research* 48 (10) (2009) 4638–4663.
- [15] J. Lu, W.-Q. Lu, A numerical simulation for mass transfer through the porous membrane of parallel straight channels, *International Journal of Heat and Mass Transfer* 53 (11–12) (2010) 2404–2413.
- [16] N.V. Gaponenko, V.S. Kortov, N.P. Smirnova, T.I. Orekhovskaya, I.A. Nikolaenko, V.A. Pustovarov, S.V. Zvonarev, A.I. Slesarev, O.P. Linnik, M.A. Zhukovskii, V.E. Borisenko, Sol–gel derived structures for optical design and photocatalytic application, *Microelectronic Engineering* 90 (2012) 131–137.
- [17] R.S. Muller, MEMS: quo vadis in century XXI? *Microelectronic Engineering* 53 (1–4) (2000) 47–54.
- [18] T.S. Leu, C.H. Cheng, M.S. Ozhgibesov, New modeling of scattering behaviors of argon atoms on tungsten substrate, *Journal of Molecular Graphics and Modelling* 31 (2011) 35–40.
- [19] F. Sharipov, Rarefied gas flow through a long rectangular channel, *Journal of Vacuum Science and Technology A* 17 (5) (1999) 3062–3066.
- [20] F.M. Sharipov, V.D. Seleznev, Rarefied gas flow through a long tube at any pressure ratio, *Journal of Vacuum Science and Technology A* 12 (5) (1994) 2933–2935.
- [21] G.A. Bird, *Molecular Gas Dynamics and the Direct Simulation of Gas Flows*, Oxford University Press/Clarendon Press, Oxford/New York, 1994.
- [22] L.A. Girifalco, V.G. Weizer, Application of the morse potential function to cubic metals, *Physical Review* 114 (3) (1959) 687–690.
- [23] M.S. Ozhgibesov, T.S. Leu, C.H. Cheng, A.V. Utkin, New statistical boundary conditions for argon–tungsten interactions, *Journal of Molecular Graphics and Modelling* 38 (2012) 375–381.
- [24] J. Yang, Y. Wang, Y. Chen, GPU accelerated molecular dynamics simulation of thermal conductivities, *Journal of Computational Physics* 221 (2) (2007) 799–804.
- [25] M.S. Friedrichs, P. Eastman, V. Vaidyanathan, M. Houston, S. Legrand, A.L. Beberg, D.L. Ensign, C.M. Bruns, V.S. Pande, Accelerating molecular dynamic simulation on graphics processing units, *Journal of Computational Chemistry* 30 (6) (2009) 864–872.
- [26] I.S. Ufimtsev, T.J. Martinez, Quantum chemistry on graphical processing units. 1. Strategies for two-electron integral evaluation, *Journal of Chemical Theory and Computation* 4 (2) (2008) 222–231.
- [27] J. Anderson, C. Lorenz, A. Travesset, General purpose molecular dynamics simulations fully implemented on graphics processing units, *Journal of Computational Physics* 227 (10) (2008) 5342–5359.
- [28] J.E. Stone, D.J. Hardy, I.S. Ufimtsev, K. Schulten, GPU-accelerated molecular modeling coming of age, *Journal of Molecular Graphics and Modelling* 29 (2) (2010) 116–125.
- [29] J.E. Stone, J.C. Phillips, P.L. Freddolino, D.J. Hardy, L.G. Trabuco, K. Schulten, Accelerating molecular modeling applications with graphics processors, *Journal of Computational Chemistry* 28 (16) (2007) 2618–2640.
- [30] M.S. Ozhgibesov, A.V. Utkin, V.M. Fomin, T.S. Leu, C.H. Cheng, Simulation of copper nanocluster deposition on the contaminated surface using gaming GPU, *International Journal of Computational Materials Science and Engineering* 1 (1) (2012) 1250007–1.
- [31] F. Sharipov, D.V. Kozak, Rarefied gas flow through a thin slit at an arbitrary pressure ratio, *European Journal of Mechanics B – Fluids* 30 (5) (2011) 543–549.
- [32] D. Chase, M. Manning, J.A. Morgan, G.M. Nathanson, R.B. Gerber, Argon scattering from liquid indium: simulations with embedded atom potentials and experiment, *The Journal of Chemical Physics* 113 (20) (2000) 9279–9287.
- [33] O.V. Sazhin, S.F. Borisov, F. Sharipov, Accommodation coefficient of tangential momentum on atomically clean and contaminated surfaces, *Journal of Vacuum Science and Technology A* 19 (5) (2001) 2499–2503.
- [34] D. Zhao, J.E. Adams, Coverage dependence of gas-surface energy transfer, *Langmuir* 1 (5) (1985) 557–564.
- [35] K.C. Janda, J.E. Hurst, C.A. Becker, J.P. Cowin, D.J. Auerbach, L. Wharton, Direct measurement of velocity distributions in argon beam–tungsten surface scattering, *The Journal of Chemical Physics* 72 (4) (1980) 2403–2410.
- [36] F. Sharipov, V. Seleznev, Data on internal rarefied gas flows, *Journal of Physical and Chemical Reference Data* 27 (3) (1998) 657–706.